

Detection of Cold Atomic Clouds in the Magellanic Bridge

Henry A. Kobulnicky^{1 2}

University of California, Santa Cruz

Lick Observatory

Santa Cruz, CA, 95064

Electronic Mail: chip@ucolick.org

John M. Dickey²

University of Minnesota, Department of Astronomy

116 Church St. SE, Minneapolis, MN 55455

Electronic Mail: john@astro.spa.umn.edu

Accepted for Publication in The Astronomical Journal

ABSTRACT

We report a direct detection of cold atomic hydrogen in the Magellanic Bridge using 21-cm absorption spectroscopy toward the radio source B0312-770. With a maximum absorption optical depth of $\tau = 0.10$ and a maximum 21-cm emission brightness temperature of 1.4 K ($N_{HI} = 1.2 \times 10^{20} \text{ cm}^{-2}$), this line of sight yields a spin temperature, T_s , between 20 K and 40 K. H I 21-cm absorption and emission spectroscopy toward 7 other low H I column density sightlines on the periphery of the LMC and SMC reveal absorption toward one additional background radio source behind the SMC with $\tau = 0.03$. The data have typical sensitivities of $\sigma_\tau = 0.005$ to 0.070 in absorption and $\sigma_{T_B} = 0.03$ K in emission. These data demonstrate the presence of a cold atomic phase which is probably accompanied by molecular condensations in the tenuous interstellar medium of the Bridge region. Young OB stars observed in the Magellanic Bridge could form *in situ* from these cold condensations rather than migrate from regions of active star formation in the main body of the SMC. The existence of cold condensations and star formation in the Magellanic Bridge might be understood as a small scale version of the mechanism that produces star formation in the tidal tails of interacting galaxies.

¹Hubble Fellow

²Visiting Astronomer, Australia Telescope National Facility, Epping, N.S.W., Australia

Subject headings: galaxies: Magellanic Clouds galaxies: Individual (LMC, SMC)
— galaxies: ISM — ISM: structure

1. Introduction

As our nearest dwarf galaxy neighbors³, the Magellanic Clouds provide the best laboratories to investigate the physical properties of the interstellar medium in relatively metal-poor environments. The impact of reduced heavy element abundances on the heating and cooling of the interstellar medium (ISM), cloud collapse, and star formation is poorly constrained from an observational standpoint. Reduced metal abundance produces the lower CO surface brightness of molecular gas in the LMC and SMC (Israel *et al.* 1993; Rubio, Lequeux, & Boulanger 1993), making the molecular phase harder to trace.

Measuring the spin temperature, T_s , of the atomic medium is one method of measuring the temperature structure of the ISM. Mebold *et al.* (1991, 1997), Braun & Walterbos (1992), Dickey & Brinks (1993), Braun (1997), and Dickey *et al.* (1994, 1998) have pioneered the study of interstellar temperatures in the Magellanic Clouds, M 31, and M 33 using this method. In the inner disk of M 31, the spin temperature of the cold neutral component of ISM appears to be similar to that in the solar neighborhood, but shows a radial gradient, averaging 70 K in the inner disk and rising to 175 K in the outer disk beyond 10 kpc (Braun & Walterbos 1992). Dickey *et al.* (1994) and Mebold *et al.* (1997) find that in the LMC the average temperature of the cold clouds is 30-40 K. While the abundance of cold clouds appears to be concentrated in regions of strong star formation like 30 Doradus, it is not yet clear from existing data whether the cold clouds in the LMC have a lower spin temperature than the Galaxy, or simply a greater volume filling factor. Contrary to results in M 31 where the spin temperatures are higher at large radii, the lowest spin temperatures measured in the LMC occur in low column density regions on the outskirts of the galaxy. A lower heating rate in the outskirts of the LMC might explain the decrease in spin temperature with radius.

In order to study the impact of environment on the formation of cold clouds and the physical conditions of the ISM, we have obtained 21-cm absorption and emission spectra

³We adopt a distance of 48 kpc to the LMC and 60 kpc to the SMC, so that 1'' corresponds to linear sizes of 0.23 pc and 0.29 pc, respectively, although the SMC apparently has a large line-of-sight depth (Wayte 1990)

along 8 lines of sight in the low column density periphery of the LMC and SMC. Figure 1 shows the locations of the background sources superimposed on a 21-cm neutral hydrogen peak brightness map of the Magellanic System (Putman *et al.* 1998). One sightline passes through the Magellanic Bridge, sampling the tenuous medium between the Clouds where we detect 21-cm absorption from cool atomic clouds. In this paper, we describe the collection and analysis of 21-cm emission spectra from the Parkes 64 m telescope and interferometric spectroscopy from the Australia Telescope Compact Array toward background radio continuum sources. We discuss the implications for the derived spin temperatures on the physical conditions in the Magellanic Bridge and on the potential for star formation in cold atomic gas clouds observed in the tidal tails of interacting galaxies.

2. Observations

2.1. Parkes Radio Telescope 21-cm Emission Line Spectroscopy

We used the Parkes 64 m radio telescope with the single-beam receiver to measure the 21-cm neutral hydrogen emission profiles toward eight background radio sources in and around the Magellanic Clouds. The observations were conducted on 1997 February 12–13, using a total bandwidth of 8 MHz and 2048 channels of 0.0039 MHz (0.82 km s^{-1}) centered at $v_{\odot} = 250 \text{ km s}^{-1}$. Due to the extended nature of HI emission around the Magellanic Clouds, all potential reference positions are contaminated by H I emission. To obtain emission-free reference spectra we interleaved on-band integrations with off-band frequency-switched ($\Delta v = 3 \text{ MHz}$) integrations centered on $v_{\odot} = 880 \text{ km s}^{-1}$, well beyond the velocity range of Magellanic H I emission. In addition to the line of sight toward the background radio source, we observed two to four adjacent positions, offset by $14'$ (slightly less than the $15'$ half-power beamwidth) in the cardinal directions. The system temperature averaged 33 K and the mean RMS noise in the resulting spectra is 0.03 K. We observed the Galactic H II region, S8, as a flux calibration standard, and scaled our temperatures to match the 76 K reported by Kalberla, Mebold, & Reif (1982).

The data for left and right circular polarization were reduced by subtracting the frequency-switched reference spectrum from the source, and fitting a low order polynomial to emission-free regions of the spectrum to remove any residual baseline. Since the Galactic and Magellanic H I emission features appear both in the signal and reference spectra, separated by 630 km s^{-1} , we are able to invert the signal and reference spectra, perform the same reduction procedure, and effectively double the integration time.

The emission spectra toward the eight sightlines appear in Figures 2a–h. The largest

source of uncertainty in the 21-cm flux and the shape of emission features associated with the Magellanic Clouds is due to ambiguities in the baseline subtraction. Narrow (<40 km s $^{-1}$) emission features brighter than 0.1 K should all be easily detected in these spectra, while broad (>100 km s $^{-1}$) low level features may be missed or mis-measured due to the baseline fitting procedure.

2.2. ATCA 21-cm Absorption Line Spectroscopy

We used the Australia Telescope Compact Array (ATCA)⁴ on 1997 January 3 in the 750A configuration to search for the 21-cm transition in absorption by cool clouds toward 8 background compact radio sources in Table 1. The target sources were selected from catalogs of known QSOs (e.g., Hewitt & Burbidge 1993) behind the LMC and SMC which had radio fluxes of at least 100 mJy in the Parkes radio survey (Otrupcek & Wright 1991). We included the V=16 QSO 0242-729 in our observing program although it did not have a previous radio detection. We avoided radio sources observed in previous Magellanic Cloud absorption-line surveys (Dickey *et al.* 1994; Dickey *et al.* 1998) which are located behind the main body of the SMC and LMC in regions of higher H I column density. Our targets have one object in common with the H I absorption survey of Mebold *et al.* (1991), B0202-765.

The ATCA correlator was configured in the FULL-4-2048 mode, yielding 2048 channels with width 1.95 kHz (0.41 km s $^{-1}$). During a 13-hour track, we observed each source for six 15-minute intervals, separated by at least 1 hour to let the earth’s rotation maximize the UV coverage. Once per hour we observed an unresolved phase calibrator, B0252-712, for five minutes. At the beginning and end of the track we observed PKS 1934-638, a standard flux and bandpass calibrator for the Compact Array. The data were reduced and calibrated in the standard manner, using the ATNF implementation of the AIPS software. The RMS noise in the bandpass solution derived from the observations of B1934-638 is 30 mJy, or 0.2% of the continuum level.

We used the AIPS task IMAGR to transform the UV visibility data into spatial maps, clean the maps to remove sidelobe structures, and produce spectral cubes with 0.82 km s $^{-1}$ channel separation. The cleaned maps have a typical RMS of 22 mJy/beam. In each field, (except B0242-729 where we find no radio continuum source to a 3σ limit of 60 mJy) we detect the background quasar which is by far the strongest radio source in the primary beam. Table 1 lists the measured flux density for each quasar, along with the flux measured

⁴The Australia Telescope is funded by the Commonwealth of Australia for operation as a National Facility funded by CSIRO

by Otrupcek & Wright (1991) in the Parkes PKSCAT90 survey. For most of the objects, the two fluxes are in excellent agreement. B2300-686 does not appear in the PKSCAT90, presumably because its flux density, as measured here by the ATCA, is at the detection limit of that survey. B0637-752 appears 1.2 Jy brighter in PKSCAT90 compared to our measurement, plausibly due to the intrinsic variability of most quasars.

All objects except B2300-683 are consistent with point sources at the resolution of our maps, typically $40''$. A Gaussian deconvolution using the synthesized clean beam suggests an intrinsic size of $60'' \times 4''$ for B2300-683 with a major axis position angle of 118° .

We extracted one-dimensional spectra toward each quasar by summing the 4-pixel region of peak flux density in each frequency plane of the spectral cube. The resulting spectra appear in Figures 2a–h, smoothed with a 3-channel boxcar for display purposes.

3. Spectral Analysis

3.1. HI Emission Profiles and Column Densities

H I emission from the Milky Way appears in all of the Parkes spectra centered near $v_\odot = 10 \text{ km s}^{-1}$. For the remainder of the analysis, we ignore the Galactic contribution to H I column densities ($v_\odot < 100 \text{ km s}^{-1}$) which is clearly separated from Magellanic Cloud velocities ($v_\odot > 150 \text{ km s}^{-1}$). Along six sightlines (B0202-765, B0242-729, B0312-770, B0506-612, B0637-752, and B2353-685) we detect an H I intensity in excess of 1 K km s^{-1} at velocities between 150 and 350 km s^{-1} corresponding to the Magellanic system. Toward 2 sources, B0743-683 and B2300-683, we achieve only upper limits of $N_{HI} < 0.1 \times 10^{19} \text{ cm}^{-2}$. In Table 2 we compile the integral brightness temperature, I_{HI} , summed across the velocity range 150–350 km s^{-1} for each line of sight. The suffixes n,s,e,w denote sightlines adjoining the primary targets, offset by $14'$ in the equatorial north, south, east, and west directions. The stated uncertainties correspond to $\sqrt{N_{channels}} \times \delta v \times \sigma_{RMS}$ where σ_{RMS} is the RMS of the offline region. This parameterization does not take into account potential systematic errors due to baseline subtraction problems or broad emission components, which, if present, would dominate the measurement uncertainties. Table 2 lists the total H I column densities along each line of sight due to the Magellanic Clouds using (Spitzer 1978)

$$N_{HI} = 1.823 \times 10^{18} \int T_B dv \text{ (cm}^{-2}\text{)} \quad (1)$$

for an optically thin medium. The data in Table 2 show that the H I column densities

vary by up to 50% at adjoining positions around the primary line of sight. This dispersion suggests the presence of significant column density variations within the primary beam. It serves as an important reminder that the large (15′) beam of the H I emission data compared to the pencil-beam nature of the absorption observations necessarily means that the two measurements refer to different volumes of the ISM and should be compared in a statistical sense only.

Using the ATCA data, we mapped each field using only UV data from the shortest baselines (applying a heavy UV taper of 5 kilo-lambda) to search for clumpy H I emission on scales smaller than the 15′ Parkes beam. Since the interferometer acts as a spatial filter, the data are insensitive to uniform emission features larger than a few arcminutes across. At 21-cm, the shortest baselines in this configuration of the ATCA are sensitive only to structures with angular sizes less than $\sim 200''$. In 7 of the 8 fields, we do not detect evidence for H I emission on scales smaller than this angular size, not even in a statistical sense. The RMS fluctuations in channels corresponding to velocities with H I emission in the Parkes spectra are identical to those in off-line channels. Only in the B0242-729 field do we find brightness fluctuations in the velocity interval 194–215 km s^{-1} , corresponding to the emission from the single dish spectra. The maps show emission from 6-8 knots with deconvolved dimensions of ~ 10 arcsec, or 2-4 pc. The maximum flux detected in any single channel is less than 0.27 Jy near 200 km s^{-1} . Assuming a gain of 0.74 K/Jy for Parkes 64 m telescope, these features would produce a brightness temperature of 0.20 K while the observed single-dish brightness temperature exceeds 6 K at this velocity (Figure 2b). Thus, only a small fraction ($< 0.2/6.2 = 3\%$) of the emission arises from compact high surface brightness structures. The low incidence of such compact structures suggests that the single dish (15′) spectra are an adequate measure of the mean H I column density in the direction of the compact radio continuum sources.

3.2. HI Absorption Spectra

Toward two sources (B0202-765 and B0312-770), we detect 21-cm absorption due to cool atomic hydrogen in the lower spin configuration of the ground $1^2S_{1/2}$ state. Along both sightlines, the velocity of the maximum optical depths ($\tau = 0.03$ and $\tau = 0.10$ respectively) agrees well with the velocity of maximum brightness temperature, T_B , suggesting that the features arise within the same physical interstellar structures. Table 2 contains the equivalent widths of the absorption features integrated across the velocity range where the absorption signature exceeds 2σ . For the six objects without observed H I absorption, we achieve 3σ upper limits on the H I optical depth between $\tau < 0.22$ and $\tau < 0.015$,

depending on the continuum source flux density. Table 2 contains the RMS optical depth sensitivity for each of the ATCA spectra.

For the two sources with measurable 21-cm absorption, we perform a more detailed analysis of the spectra by fitting Gaussian components to the emission and absorption features. B0312-770 exhibits three clear components in both emission and absorption. In Table 2 we list the integrated brightness temperatures or optical depths, the center velocities, FWHM, and peak amplitudes for each of the components individually. We fit all 3 components simultaneously, allowing the position, amplitude, and width to vary as free parameters. Attempts to use only two components result in large residuals, while using four or more components does not significantly improve the fit. Of course, many narrow, blended components may produce the observed spectra, but with the current spectral resolution and limited signal-to-noise, there is no warrant for using more than 3 components in the fit.

For B0202-765 two Gaussian components produce an excellent fit to the emission spectrum. The dominant component is centered at $v_{\odot} = 161.8 \text{ km s}^{-1}$ and a much weaker component appears at $v_{\odot} = 197.8 \text{ km s}^{-1}$. For the absorption spectrum, the situation is more complicated. A single component fit centered at $v_{\odot} = 156.1 \text{ km s}^{-1}$ has large residuals. Adding a second component results in slightly smaller residuals and yields center velocities of $v_{\odot} = 146.6$ and $v_{\odot} = 162.7 \text{ km s}^{-1}$ for the two features. Adding a third component significantly improves the fit. The three absorption components are centered at $v_{\odot} = 137.4 \text{ km s}^{-1}$, 147.6 km s^{-1} , and 162.1 km s^{-1} . The velocity of the dominant component at $v_{\odot} = 162.1 \text{ km s}^{-1}$ agrees well with the velocity of the main emission component. One reasonable interpretation is that the interstellar H I structure producing the dominant emission component contains three separate cold inclusions at different velocities which give rise to the three absorption components. If there exists cold atomic gas associated with the weaker emission component at $v_{\odot} = 197.8 \text{ km s}^{-1}$ it must be below our detection threshold of $\sigma_{\tau} = 0.01$.

4. The Physical Conditions of Gas in the Magellanic Bridge

Measurements of the 21-cm emission and absorption profiles along the same line of sight provide an estimate of the spin temperature, T_s , of the neutral atomic medium. However, any given sightline will sample a mixture of physical components, including the diffuse ionized gas, the warm and cold neutral medium, and even the dense molecular phase. In the Milky Way, neutral hydrogen exists predominantly (75%) in the warm (200 K) neutral phase. The results in other galaxies are mixed, with M 31 having 65% in the warm phase, and M 33 having 85% (Dickey & Brinks 1993). The results for the LMC are consistent with

the Milky Way, except for the 30-Doradus region which appears to have an excess of cold atomic clouds (Dickey *et al.* 1994). The SMC shows spin temperatures between 20 and 50 K (Dickey *et al.* 1999). However, the low column density regions between the Magellanic Clouds have not yet been probed. The radio source B0312-770 lies behind the Magellanic Bridge and offers an opportunity to probe its thermodynamic state.

Using the data from Table 2, we explore several methods for finding the spin temperature of the gas, T_s . In the second column of Table 3, we calculate a “mean spin temperature” along each line of sight using

$$\langle T_s \rangle = \frac{\int T_B dv}{\int 1 - e^{(-\tau)} dv} \simeq \frac{\int T_B dv}{\int \tau dv}. \quad (2)$$

This algorithm sums all the gas along the line of sight. It does not distinguish emission from the warm ISM associated with the cold absorption features from other, unaffiliated warm gas along the same line of sight. Thus, it provides an upper limit on the spin temperature of the cold neutral medium. We find mean spin temperatures of 87 ± 7 K and 32 ± 4 K for B0202-765 and B0312-770 respectively. Computing a mean spin temperature for each well-defined absorption/emission feature in these two sources yields 143 ± 19 K for component 3 in B0202-765 and 22–46 K for the three components in B0312-770.

Another approach uses only the emission brightness temperature and maximum optical depth of associated emission/absorption components which co-incide at velocity v_0 . In the third column of Table 3 we list the “central spin temperature” defined by

$$T_s(v_0) = \frac{T_B(v_0)}{(1 - e^{-\tau(v_0)})}, \quad (3)$$

where v_0 is center velocity of each absorption component in Table 2, and $T_B(v_0)$ is the brightness temperature interpolated at v_0 . The resulting spin temperatures using this approach are lower than for the line integral algorithm since it is less sensitive to emitting gas at different velocities which is presumably not affiliated with the absorbing component. However, if different warm and cold gas components overlap in velocity space, then even this method measures only the ensemble average of the physical properties. Using this approach, we find spin temperatures of 8 K, 38 K, and 68 K for the three components toward B0202-765 and 6 K, 38 K, and 14 K toward B0312-770.

Mebold *et al.* (1997) develop a more sophisticated method for measuring the spin temperature of the ISM by separating the warm and cold components. Cold, absorbing gas clouds are usually embedded amidst more extended complexes of warm neutral gas

responsible for the emission. An accurate measurement of the spin temperature requires separating the emission affiliated with the absorbing components from emission produced by more extended, unrelated gas. In Figures 3 and 4 we plot the emission brightness temperature, T_B , versus the absorption ($1 - e^{-\tau} \sim \tau$ for the small optical depths studied here) on a per-channel basis. We compute the emission brightness temperature at the velocity of the absorption velocity channels using a cubic spline interpolation. A cross marks each channel. A dotted line connects channels with emission brightness temperature greater than 2σ , while a solid line connects four or more consecutive channels with absorption at greater than the 2σ level. Radial lines from the origin denote the loci of constant spin temperature. Parcels of warm gas without absorbing components cause the sequence of connected points to make an excursion in the vertical direction. Absorbing gas clouds with measurable optical depth cause the series of connected points to make an excursion to the right (solid lines). In the method outlined by Mebold *et al.* the slope, m , of a linear fit to the absorbing channels outlined by the solid lines yields the spin temperature of the cold component alone, T_{sc} . The intercept of this linear fit with the y-axis yields the emission brightness temperature, T_{EW} , of the unaffiliated warm gas. Our attempts to measure the spin temperature of the cold component alone using this method yield unphysically low (even negative) values. The unphysical results are probably because large beamsize of the emission observations is poorly matched to the scale of the individual absorbing material, and there is only a statistical correlation between absorption and emission properties of any particular velocity channel. Consequently, we proceed no further with this type of detailed analysis

4.1. Comments on Individual Objects

B0202-765: Mebold *et al.* (1991) presented ATCA spectroscopy toward this source, and they detected no absorption to a level of $\tau > 0.044$. Our new data have four times the sensitivity of that presented in Mebold *et al.*. We detect absorption with a maximum optical depth of $\tau = 0.025$ in the strongest component.

B0242-729: Although this sightline contained no known radio source in previous single-dish radio surveys, we included this field because it contains an optically bright background QSO. We find no radio continuum source to a 3σ limit of 66 mJy.

B0312-770: Situated behind the Magellanic Bridge, this source allows us to probe the physical conditions in the tenuous Bridge medium. The H I contour maps of Mathewson & Ford (1984) indicate an H I column density between 1×10^{20} and $5 \times 10^{20} \text{ cm}^{-2}$ while our pointed observations better constrain this value to within $1\text{--}2 \times 10^{20} \text{ cm}^{-2}$.

B0637-752: Bowen, Blades, & Pettini (1995) detected two strong Mg II $\lambda\lambda 2796, 2803$ absorption components toward this quasar at velocities of 250 km s^{-1} and 320 km s^{-1} with equivalent widths of 1.4 \AA and 1.1 \AA . The H I emission spectrum in Figure 2g shows a component near 250 km s^{-1} and a secondary component near 290 km s^{-1} , but no feature corresponding to the Mg II absorption at 320 km s^{-1} . Adopting the mean LMC distance of 49.4 kpc used by Bowen *et al.*, this sightline intersects the LMC at a radius of 6.7 kpc where we measure an H I columns density of $2.1 \times 10^{19} \text{ cm}^{-2}$. At this radius, Dickey *et al.* (1994) find spin temperatures in excess of 200 K , or possibly as high as 3000 K adopting their linear relation between radius and spin temperature. This is consistent with our lower limit of $T_S > 380 \text{ K}$.

B2353-685: We note the possible presence of an H I absorption feature with maximum optical depth $\tau = 0.06$ near $v_{\odot} = 285 \text{ km s}^{-1}$ in Figure 2h. There is no detectable 21-cm emission at corresponding velocities. Optical or ultraviolet spectra toward this QSO would be valuable to search for metal absorption lines which may indicate the presence of a small, cold intergalactic cloud.

4.2. Implications of the Measured Spin Temperatures

In the Milky Way, requiring that the heating and cooling rates be equal prescribes an equilibrium curve for density and temperature. The cooling rate increases as density squared since cooling processes depend on collisions in the gas, (e.g., excitation of fine structure lines) or recombination of electrons onto ions or charged grains. Heating typically depends on density to the first power, since it is proportional to the ionization rate due to cosmic rays or X-rays, or to the photoelectron emission rate from grains. The gas is forced to the cool phase if the density is high, since the cooling rate will exceed the heating rate, unless the gas is so cold that collisions seldom excite the fine structure line of O I. For gas temperatures below 100 K the dominant coolants are C II and C I fine structure lines. In the Milky Way, for a given ISM pressure, there is a range of densities for which the equilibrium is unstable. Stable equilibria are possible only if the gas density is below about 0.5 cm^{-3} or above about 5 cm^{-3} , corresponding to temperatures above 6000 K and below 150 K respectively (Field, Goldsmith & Habing, 1969; reviewed by Wolfire *et al.* 1995).

Reducing the metallicity of the gas effects both the heating and cooling processes, since in the cool phase the dominant heating process is photoelectron emission from grains. In the SMC the dust to gas ratio is low by roughly an order of magnitude compared to the Milky Way (Schwering 1989) and the abundance of C and O in the gas is low by a factor of 8 (Pagel *et al.* 1978). Wolfire *et al.* (1995) consider how changing the metallicity of the

medium changes the equilibrium curve of heating-cooling balance. They find that for an increasingly metal-poor medium where the dust-to-gas ratio varies as the metallicity, the loss of coolants is more important than the loss of grains for heating. The warm phase becomes more dominant, in the sense that the minimum pressure for which the cool phase is possible increases. The maximum pressure for which the warm phase is possible also increases.

Spin temperatures of 20 to 50 K have been measured for HI clouds in the SMC by Dickey *et al.* (1998), thus the temperatures measured for the Bridge gas here are similar to these SMC values. In the Magellanic Bridge the pressure must be very low on average, since there is no steep gradient in the gravitational potential to confine gas at high pressures, but the presence of cool HI clouds shows that some regions must be at high densities. Assuming a metallicity $Z = 0.15Z_{\odot}$ which is typical of nebulae in the SMC (Pagel *et al.* 1978), the minimum density which allows a cool phase is about 10 cm^{-3} (Wolfire *et al.* 1995; their Figure 6). For temperatures as low as 25 to 50 K, the density must be considerably higher, probably above 100 cm^{-3} , if the gas is in thermal equilibrium. This implies a pressure of $3 \times 10^3 \text{ cm}^{-3} \text{ K}$ for a temperature of 30 K. The question is how to confine clouds with this pressure. It may be that this part of the Bridge is a region where streamlines cross, meaning that the interaction between the Clouds, and between the Clouds and the Milky Way, has led to gravitational focusing of the gas trajectories in the Bridge region. There may be a shock in the low density Bridge gas, with these cool clouds tracing the post-shock material.

4.3. Implications for Star Formation in the Magellanic Bridge

The dynamical structure of the Magellanic Clouds is complex, probably due to previous close interactions with each other, and with the Milky Way (Mathewson & Ford 1984; Murai & Fujimoto 1980). At least two separate velocity components comprise the Magellanic system, and the SMC has a large depth along the line of sight, perhaps 20 kpc, suggesting that it is in the process of being disrupted (Wayte 1990; Mathewson, Ford, & Visvanathan 1986, 1988). The bridge of neutral hydrogen connecting the LMC and SMC (Hindman, Kerr, & McGee 1963; Putman *et al.* 1998) is probably material that has been tidally stripped from one of the galaxies, but its origin, thermodynamic state, and metallicity are poorly known.

The Magellanic Stream exhibits both diffuse H α emission (Johnson, Meaburn, & Osman 1982; Meaburn 1986) and associations of young blue stars in the eastern wing (Shapley 1940; $\alpha = 2^h 15^m$, $\delta = -74^\circ$) of the SMC and in the Bridge between the Clouds (Courtes *et al.* 1995; Grondin, Demers, & Kunkel 1992; Demers *et al.* 1991; Grondin *et al.*

1990; Irwin, Demers, & Kunkel 1990). Some of these clusters contain early B type stars with main sequence lifetimes as short as 20 Myr. They are located 5° (~ 5 kpc) from the dominant star-forming regions in the SMC, leading to speculation about their origin. Have these young stars migrated from regions of more vigorous star formation or have they formed *in situ* from gas comprising the Bridge? In order to travel 5 kpc in 20 Myr, these stars must have extremely large peculiar velocities in excess of 250 km s^{-1} . An alternative interpretation is that new stars, including massive stars, are currently forming in the Magellanic Bridge. The correlation between H I column density and the density of young OB associations in the Bridge (Battinelli & Demers 1992) is consistent with this later hypothesis. In all known environments, star formation is observed to occur within molecular clouds or cloud complexes, but there is presently no direct evidence of star-forming gas clouds in the Bridge.

In lieu of millimeter-wave CO data which directly reveals the presence of molecular gas, H I 21-cm absorption traces the cold (30–40 K) atomic medium which is associated with molecular clouds in the Galaxy where the ratio of atomic to molecular column density, N_{HI}/N_{H_2} , is $\sim 0.02 - 0.2$ (Despois & Baudry 1985). The detection of such cold cloud conditions even in an area of relatively low H I column density toward B0312-770 ($1 \times 10^{20} \text{ cm}^{-2}$) strongly suggests the presence of atomic or molecular condensations which could harbor star formation. The B0312-770 sightline passes just south of the Bridge regions searched by Bottinelli & Demers (1992) and Irwin *et al.* (1990) for OB associations, so we cannot test whether this particular ISM feature corresponds to a stellar association.

5. Conclusions

We present H I 21-cm emission and absorption measurements toward 8 sightlines in the periphery and Bridge region of the Magellanic Clouds. Toward two of the background radio sources, we detect measurable 21-cm absorption which indicates the presence of cold atomic gas with spin temperatures between 20 K and 40 K. The presence of cold atomic condensations in the relatively low column density outlying regions of the Clouds is direct evidence for the raw material of star formation. If the young OB associations observed in the Magellanic Bridge region formed *in situ*, then our nearest neighbor galaxies offer a laboratory for studying the star formation process in the tidal tails and streamers produced during galactic interactions. This result underscores the need for a more thorough study of the thermodynamic properties of the gas and of the stellar populations in the Magellanic Bridge.

We thank Mary Putman for producing the 21-cm H I map of the Magellanic System for Figure 1 and Snezana Stanimirovic for help with the data collection and reduction. H. A. K. thanks the Guillermo Haro International Program for Advanced Studies in Astrophysics at the Instituto Nacional de Astrofisica Optica y Electronica (INAOE) in Puebla, Mexico for hospitality during the 1998 summer workshop on galaxy evolution during which much of this paper was written. H. A. K. is grateful for assistance from a NASA Graduate Student Researchers Program fellowship and from NASA through grant #HF-01094.01-97A awarded by the Space Telescope Science Institute which is operated by the Association of Universities for Research in Astronomy, Inc. for NASA under contract NAS 5-26555. This research has made use of the NASA/IPAC Extragalactic Database (NED) which is operated by the Jet Propulsion Laboratory, California Institute of Technology, under contract with the National Aeronautics and Space Administration.

REFERENCES

- Battinelli, P., & Demers, S. 1992, *AJ*, 104, 1458
- Bowen, D. V., Blades, J. C., & Pettini, M. 1995, *ApJ*, 448, 634
- Braun, R., & Walterbos, R. A. M. 1992, *ApJ*, 386, 120
- Braun, R., 1997, *ApJ*, 484, 637
- Courtes, G., Viton, M., Bowyer, S., Lampton, M., Sassuun, T. P., & Wu, X.-Y. 1995, *A&A*, 297, 338
- Demers, S., Grondin, L., Irwin, M. J., & Kunkel, W. E. 1991, *AJ*, 101, 911
- Despois, D., & Baudry, A. 1985, *A&A*, 148, 83
- Dickey, J. M., & Brinks, E. 1993, *ApJ*, 405, 153
- Dickey, J. M., Mebold, U., Marx, M., Amy, S., Haynes, R. F., & Wilson, S. 1994, *A&A*, 289, 357
- Dickey, J. M., *et al.* 1999, in prep
- Field, G. B., Goldsmith, D. W., & Habing, H. 1969, *ApJ*, 155, L49
- Grondin, L., Demers, S., & Kunkel, W. E. 1992, *AJ*, 103, 1234
- Grondin, L., Demers, S., Kunkel, W. E. & Irwin, M. J. 1990, 100, 663
- Hewitt, A. & Burbidge, G. 1993, *ApJS*, 87, 451
- Hindman, J. V., Kerr, F. J., & McGee, R. X. 1963, *Aust. J. Phys.*, 16, 570
- Irwin, M. J., Demers, S., & Kunkel, W. E. 1990, *AJ*, 99, 191

- Israel, F. P., Johansson, L. E. B., Lequeux, J., *et al.* 1993, A&A, 276, 25
- Johnson, P. G., Meaburn, J., & Osman, A. M. 1982, MNRAS, 198, 985
- Kalberla, P. W. M., Mebold, U., & Reif, K. 1982, A&A, 106, 190
- Mathewson, D. S., Ford, V. L. 1984, in IAU Symposium 108, Structure and Evolution of the Magellanic Clouds, ed S. van den Bergh and K.S. de Boer (Dordrecht: Reiderl), p. 125
- Mathewson, D. S., Ford, V. L., & Visvanathan, N. 1986, ApJ, 301, 664
- Mathewson, D. S., Ford, V. L., & Visvanathan, N. 1988, ApJ, 333, 617
- Meaburn, J. 1986, MNRAS, 223, 317
- Mebold, U., Greisen, E. W., Wilson, S., Haynes, R. F., Herbstmeier, U., & Kalberla, P. M. W. 1991, A&A, 251, L1
- Mebold, U., Düsterberg, C., Dickey, J. M., Staveley-Smith, L., & Kalberla, P. 1997, ApJ, 490, L65
- Murai, T., & Fujimoto, M. 1980, PASJ, 32, 581
- Otrupcek, R., & Wright A. E. 1991, PASAu 9, 170
- Pagel, B. E. J., & Edmunds, M. G., Fosbury, R. A. E., & Webster, B. L. 1978, MNRAS, 184, 569
- Putman, M. E., *et al.* 1998, Nature, 394, 752
- Rubio, M., Lequeux, J., & Boulanger, F. 1993, A&A, 271, 9
- Schwering, P. B. W. 1989, A&AS 79, 105
- Shapley, H. 1940, Harvard Obs. Bull., 814, 8
- Spitzer, L. Jr. 1978, Physical Process in the Interstellar Medium (New York:Wiley), 43
- Wayte, S. R. 1990, ApJ, 355, 473
- Wolfire, M. G., Hollenbach, D., McKee, C. F., Tielens, A. G. G. M, & Bakes, E. L. O. 1995, ApJ, 443, 152

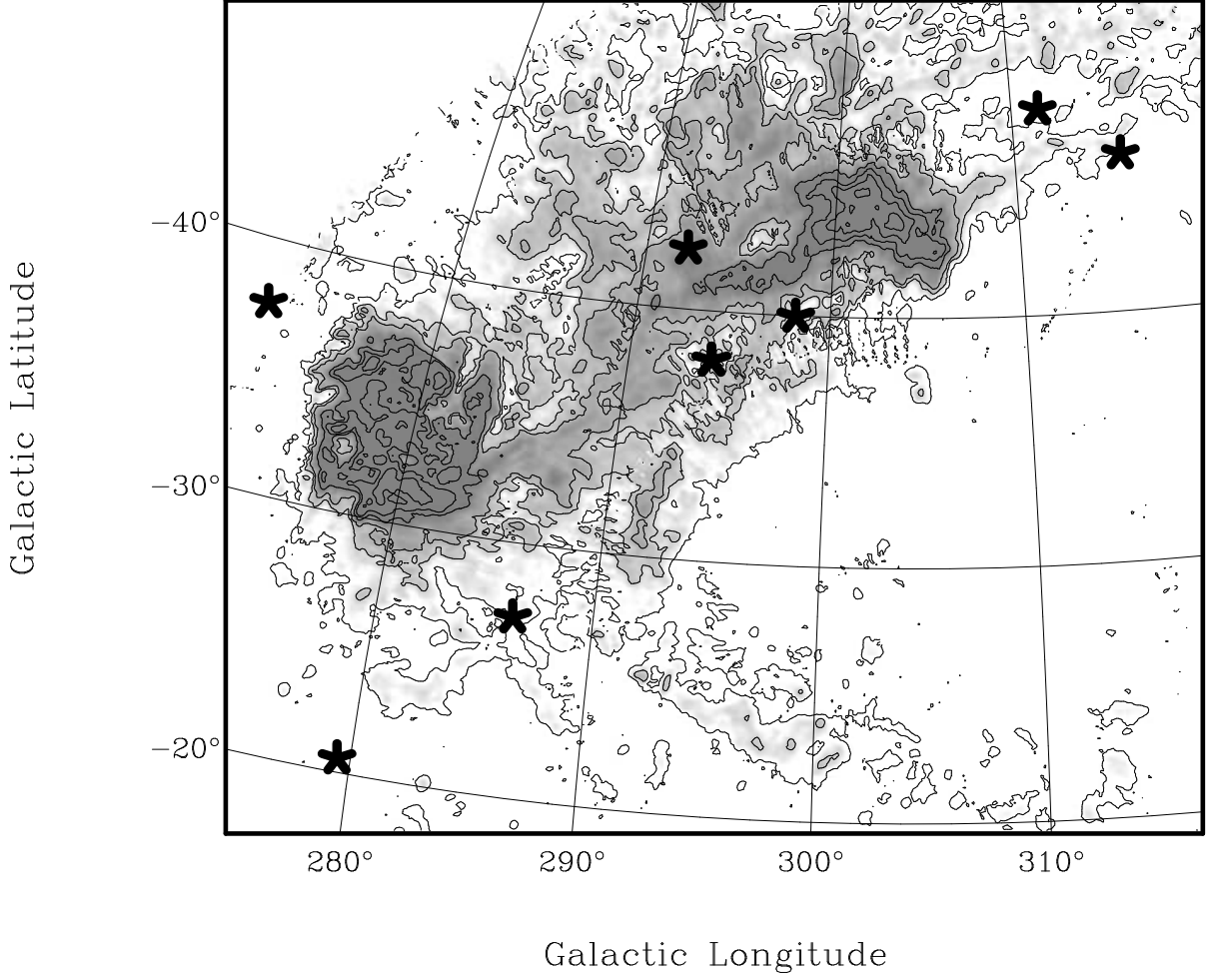


Fig. 1.— H I peak brightness temperature map of the Magellanic Clouds from Putman *et al.* (1998). Contours mark the 0.1 K (5σ), 0.8, 2, 8, 16, 32, 64, and 128 K peak brightness. Asterisks mark the lines of sight toward background radio sources listed in Table 1. Two radio sources lie behind the Magellanic Bridge, while the others lie on the extreme periphery of the Clouds along lines of sight with low H I column density ($N_{HI} < 4 \times 10^{19} \text{ cm}^{-2}$).

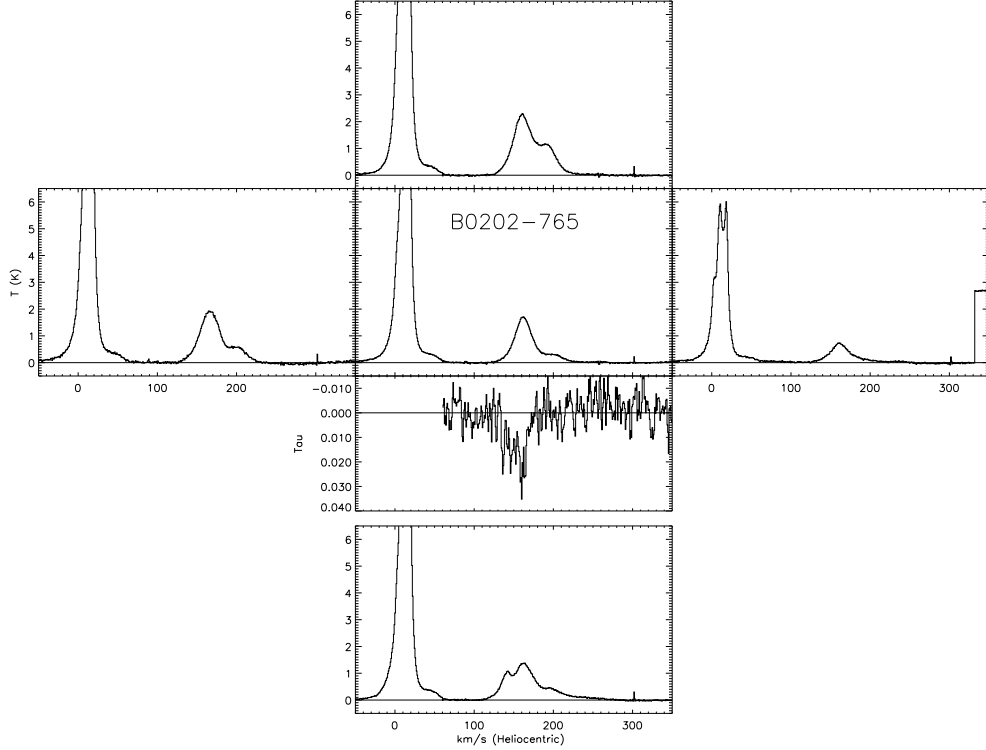


Fig. 2.— a: 21-cm emission and absorption spectra along 8 lines of sight toward the Magellanic Bridge and around the periphery of the LMC and SMC. The central panel in each figure shows the H I emission spectrum from the Parkes 64 m antenna toward the background radio source. Absorption spectra against the background radio sources obtained with the Australia Telescope Compact Array appear just below the central panel. Flanking emission spectra show the H I profiles offset by $14'$ to either side of the primary sightline. The channel width of the absorption and emission data is 3.9 kHz (0.82 km s^{-1}). The absorption spectra have been smoothed with a 3-pixel boxcar for display purposes.

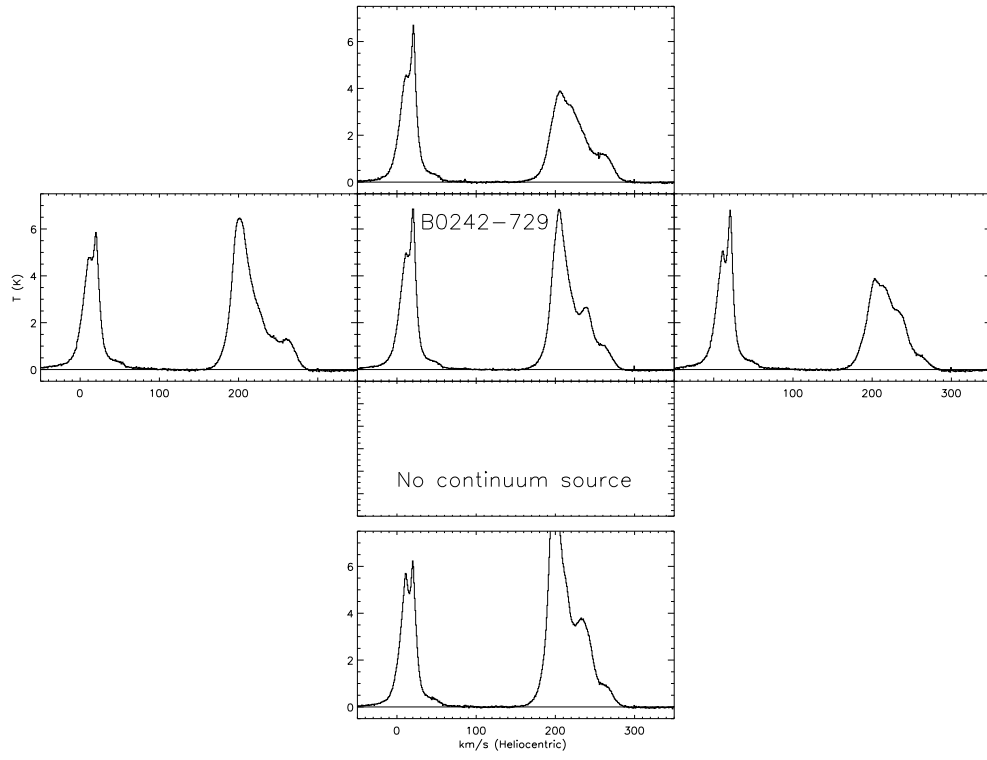


Fig. 2b

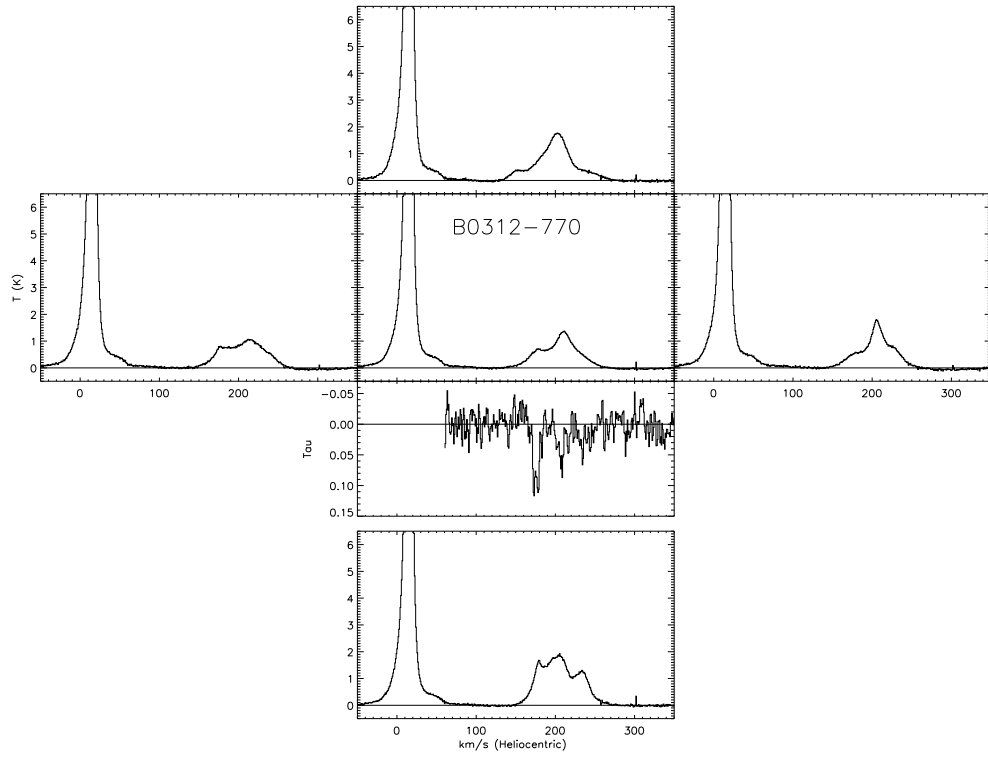


Fig. 2c

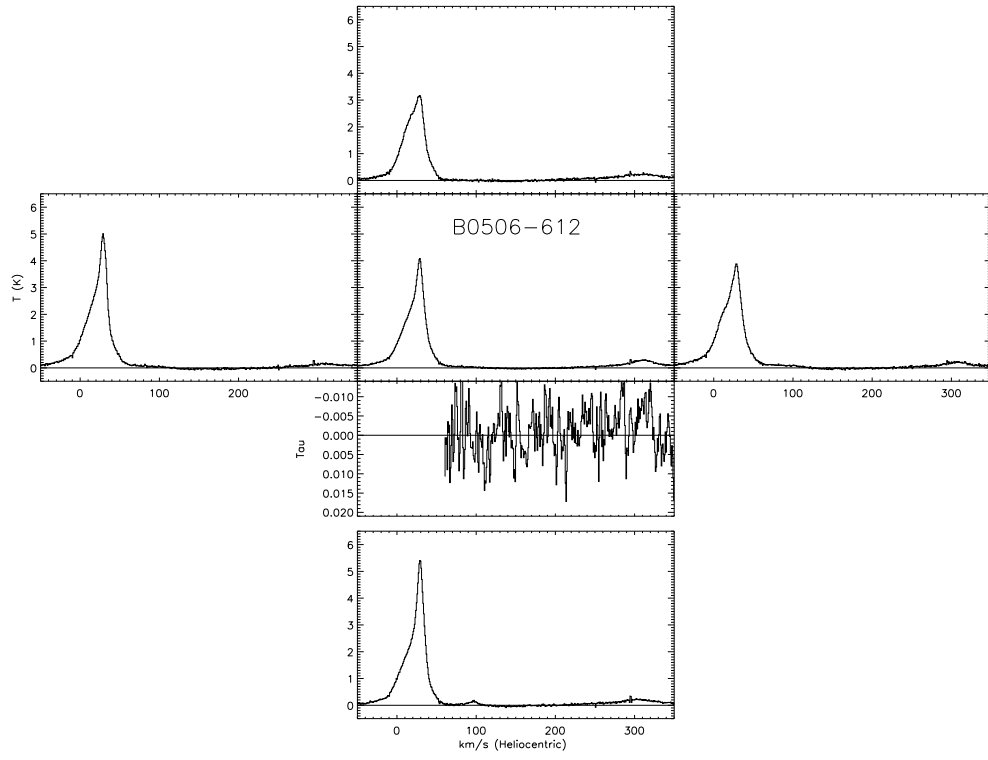


Fig. 2d

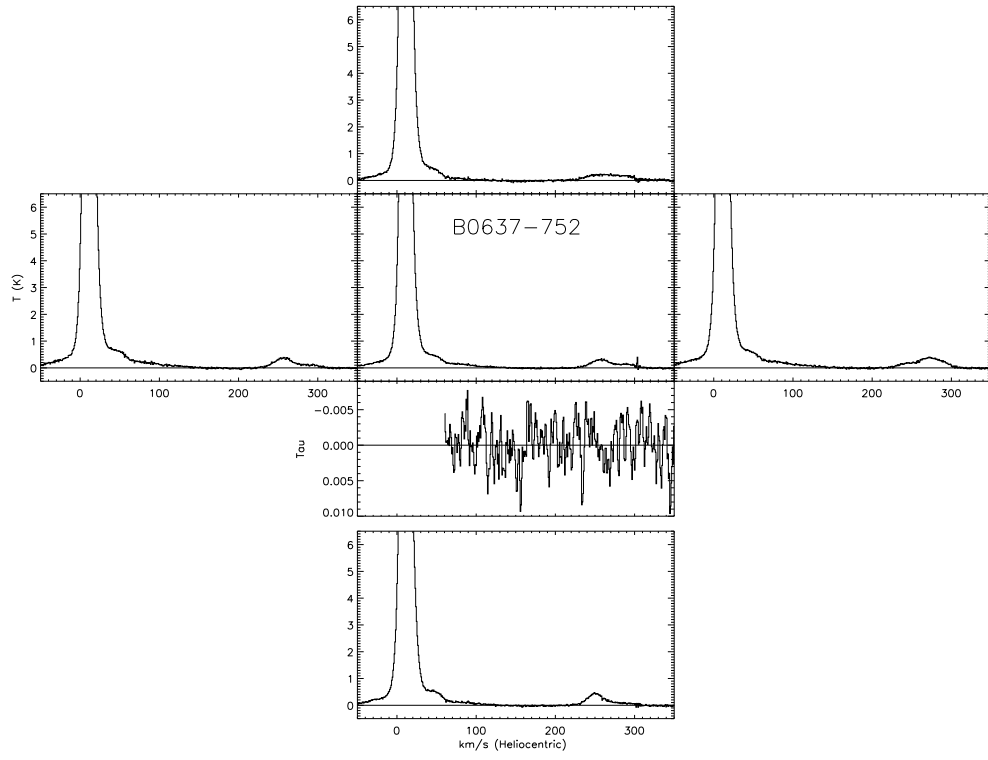


Fig. 2e

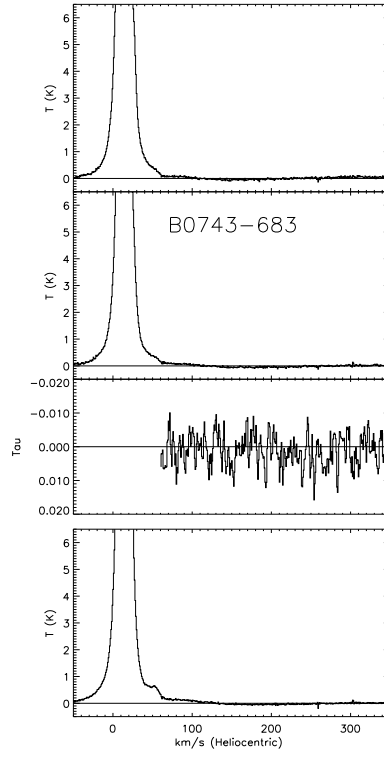


Fig. 2f

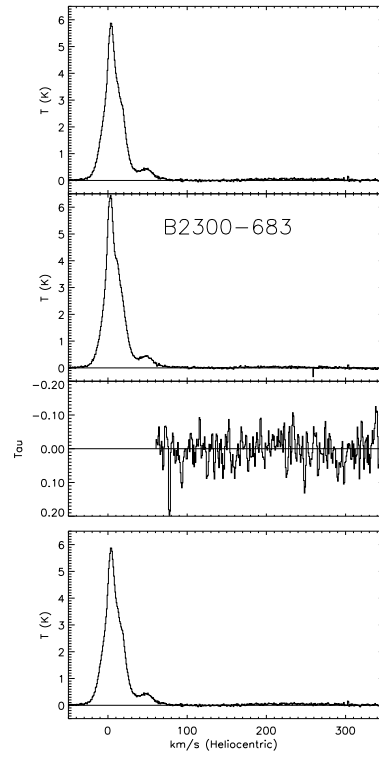


Fig. 2g

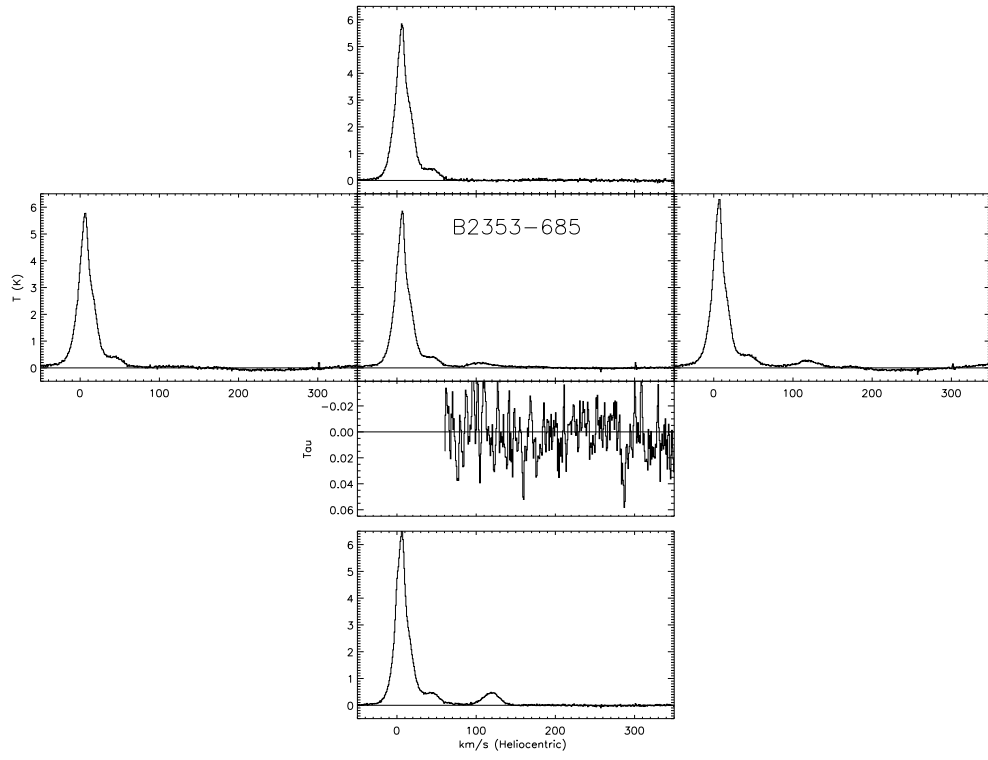


Fig. 2h

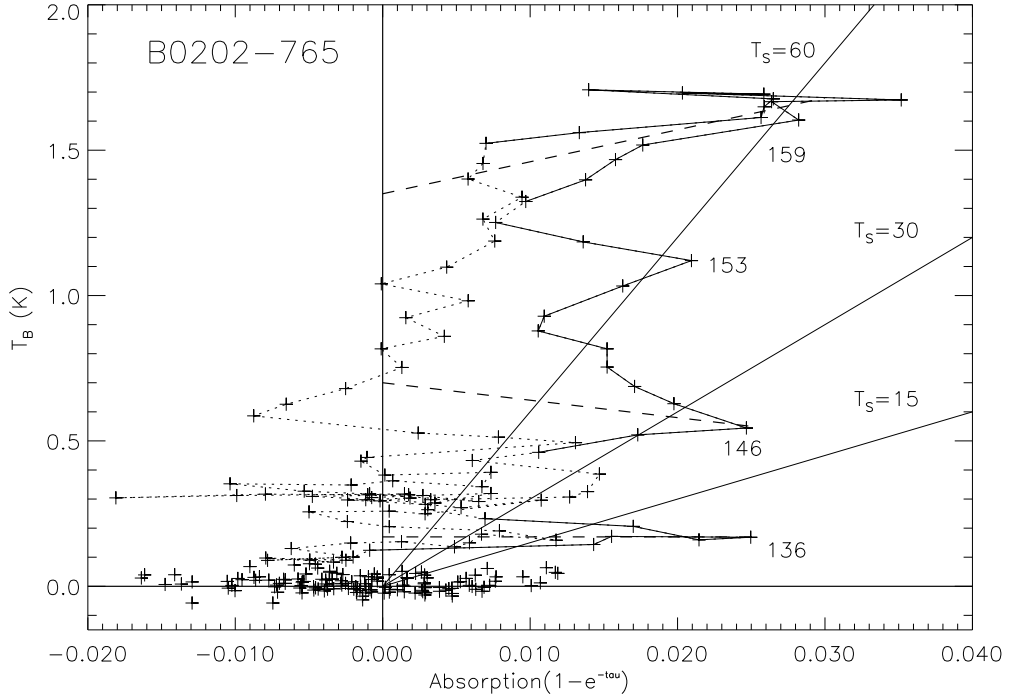


Fig. 3.— The H I emission brightness temperature, T_B , versus absorption ($1 - e^{-\tau}$) for each 0.82 km s^{-1} velocity channel (crosses) in the B0202-765 spectra. Velocity intervals with measurable absorption appear connected by solid lines, while regions of measurable emission appear connected by dotted lines. Numbers adjacent to the symbols give the heliocentric velocity of the channel. Solid lines from the origin illustrate the loci of constant spin temperature, T_s . Dashed line segments show the fit to specific absorption features and are used to derive the spin temperature of the cold atomic component.

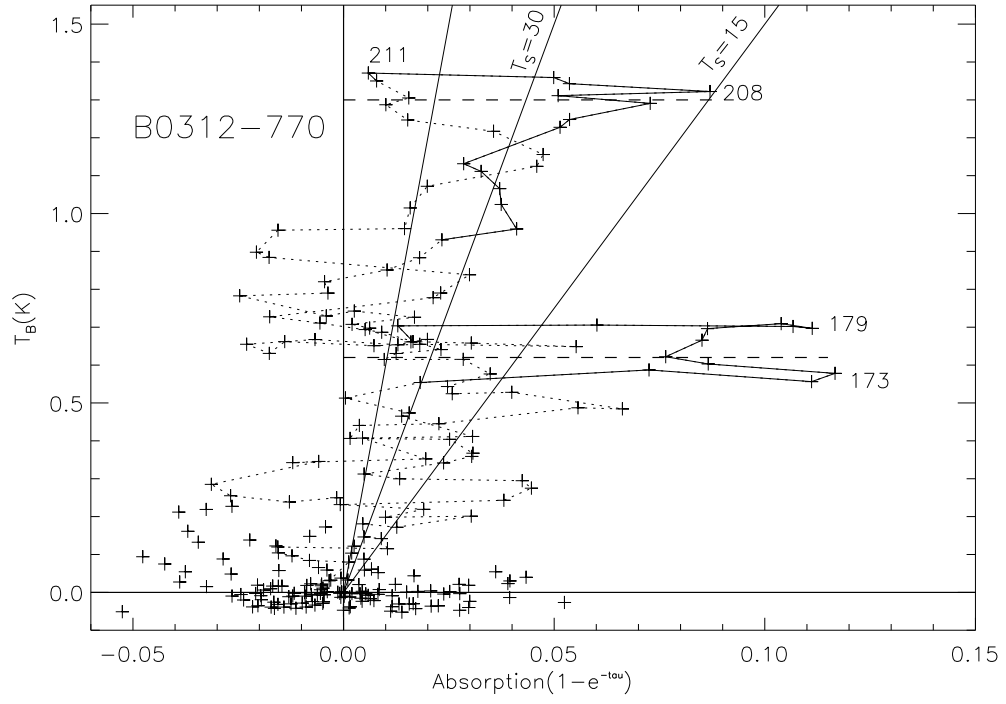


Fig. 4.— Same as Figure 3 for the sightline toward B0312-770.

TABLE 1
LOG OF PARKES AND ATCA 21-CM OBSERVATIONS

Object	RA (2000) ^a	DEC (2000) ^a	Flux (mJy) ^b	Flux (mJy) ^c	B mag.
B2300-683	23 03 44.18	-68 07 45.5	320	...	16.4
B2353-686	23 56 05.93	-68 18 41.9	960	1180	17.9
B0202-765	02 02 13.08	-76 20 05.3	2340	2440	16.0
B0242-729	02 43 09.59	-72 16 48.9	<66 ^d	...	16.
B0312-770	03 11 54.75	-76 51 51.6	610	620	17.2
B0506-612	05 06 44.10	-61 09 40.9	2010	2000	17.9
B0637-752	06 37 46.53	-75 16 17.1	3730	4940	17.2
B0743-673	07 43 32.35	-67 26 25.6	5320	5300	17.0

^aOptical position

^bMeasured ATCA flux density for the radio source mapped with a synthesized beamsize of $\sim 40''$

^cFlux from Parkes PKSCAT90 catalog (Otrupcek & Wright 1991)

^d 3σ upper limit

TABLE 2
21-CM EMISSION AND ABSORPTION LINE PROFILE DATA

Object	Emission $\int T_B dv^a$ K km s ⁻¹	N_{HI} $\times 10^{19}$ cm ⁻²	V_\odot km s ⁻¹	FWHM km s ⁻¹	Peak K	Absorption EW km s ⁻¹	V_\odot km s ⁻¹	FWHM km s ⁻¹
(1)	(2)	(3)	(4)	(5)	(6)	(7)	(8)	(9)
B2300-683	<0.6 ^a	<0.11 ^a	<0.05	<0.45 ^b
B2300-683n	<0.6 ^a	<0.11 ^a	<0.05
B2300-683s	<0.6 ^a	<0.11 ^a	<0.05
B2353-685	8.08±0.15	1.47±0.03	0.21	<0.15 ^b
B2353-685n	1.79±0.13	0.37±0.02	0.10
B2353-685s	11.40±0.11	2.08±0.02	0.49
B2353-685e	0.0±0.22	0.0±0.04	0.11
B2353-685w	6.97±0.19	1.27±0.03	0.29
B0202-765	55.98±0.31	10.24±0.06	1.71	0.62±0.05
comp 1	0.07±0.01	137.4	3.0
comp 2	0.19±0.03	147.6	10.0
comp 3	44.60±0.10	8.16±0.18	161.8	25.5	1.63	0.31±0.04	162.0	11.1
comp 4	9.95±0.07	1.82±0.12	197.8	31.2	0.30
B0202-765n	96.34±0.16	17.63±0.03	2.30
B0202-765s	71.05±0.39	13.00±0.07	1.38
B0202-765e	74.54±0.46	13.64±0.08	1.93
B0202-765w	24.83±0.35	4.54±0.06	0.74
B0242-729	251.74±0.50	46.07±0.09	6.94
B0312-770	65.40±0.38	11.97±0.07	1.37	2.05±0.26
comp 1	24.30±0.38	4.44±0.69	181.1	33.5	0.68	1.08±0.07	175.8	9.6
comp 2	22.17±0.37	4.05±0.68	209.6	20.8	1.00	0.77±0.07	206.9	13.2
comp 3	19.65±0.10	3.59±0.18	227.9	34.9	0.53	0.43±0.07	234.6	10.5
B0312-770n	84.78±0.40	15.51±0.07	1.77
B0312-770s	110.89±0.48	20.29±0.09	1.93
B0312-770e	66.38±0.44	12.14±0.08	1.08
B0312-770w	66.84±0.41	12.23±0.07	1.81
B0506-612	19.01±0.27	3.47±0.05	0.30	<0.07 ^b
B0506-612n	20.71±0.45	3.79±0.08	0.34
B0506-612s	17.51±0.52	3.20±0.09	0.34
B0506-612e	12.83±0.33	2.34±0.06	0.27
B0506-612w	14.27±0.29	2.28±0.06	0.27
B0637-752	11.48±0.28	2.10±0.06	0.35	<0.03 ^b
B0637-752n	13.36±0.32	2.44±0.06	0.26
B0637-752s	12.76±0.29	2.33±0.06	0.47
B0637-752e	12.74±0.46	2.33±0.08	0.39
B0637-752w	16.59±0.26	3.03±0.05	0.40
B0743-683	<0.6 ^a	<0.11 ^a	<0.05	<0.05 ^b
B0743-683n	<0.6 ^a	<0.11 ^a	<0.05
B0743-683s	<0.6 ^a	<0.11 ^a	<0.05

TABLE 2—*Continued*

Object	Emission				Absorption				
	$\int T_B dv^a$ K km s ⁻¹	N_{HI} $\times 10^{19}$ cm ⁻²	V_\odot km s ⁻¹	FWHM km s ⁻¹	Peak K	EW km s ⁻¹	V_\odot km s ⁻¹	FWHM km s ⁻¹	τ_{max}
(1)	(2)	(3)	(4)	(5)	(6)	(7)	(8)	(9)	(10)

¹Object Name. Where multiple velocity components can be defined, they are listed separately.

²21-cm emission line integral from 100 km s⁻¹ — 350 km s⁻¹ or the integral of the best-fit Gaussian profile in the case of individual components.

³HI column density derived from column 1 assuming N_{HI} (cm⁻²) = $1.823 \times 10^{18} \int T_B dv$ for an optically thin medium.

⁴The center velocity of best-fit Gaussian components to the emission spectrum in the heliocentric reference frame.

⁵The full width half max of the best-fit Gaussian components in km s⁻¹.

⁶The peak 21-cm brightness temperature from the Parkes 64 m spectra. The listed value corresponds to the maximum T_B or the maximum of the Gaussian fit in the case of individual components.

⁷The absorption equivalent width. The listed value corresponds to the global line integral, $\int \tau dv$, or the integral of the best fit Gaussian profile in the case of individual components.

⁸The center velocity of the best-fit Gaussian profile for individual absorption components.

⁹The full width at half depth of the best-fit Gaussian profile for absorption components.

¹⁰Maximum optical depth. The listed value corresponds to the global maximum in the optical depth, or the maximum of the Gaussian fit in the case of individual components.

¹¹Channel-to-channel RMS noise in the raw, 0.82 km s⁻¹ unsmoothed spectra. For display purposes, the absorption spectra are smoothed with a 3-pixel boxcar in the Figures where the RMS appears a factor ~ 2 lower.

^a 3σ upper limit

^b 3σ upper limit for an assumed line width of 3.3 km s⁻¹ (4 channels)

TABLE 3
DERIVED PROPERTIES OF ABSORPTION-LINE SOURCES

Object	$\langle T_s \rangle$	$T_s(v_0)$
	K	K
(1)	(2)	(3)
B2353-685	>42	>7
B0202-765	87 ± 7	...
comp 1	...	8
comp 2	...	38
comp 3	143 ± 19	68
B0312-770	32 ± 4	...
comp 1	22 ± 2	6
comp 2	29 ± 3	38
comp 3	46 ± 7	14
B0506-612	>270	>27
B0637-752	>380	>70

¹Object Name. Fits to individual components are listed separately.

²The ensemble average spin temperature. computed from $\int T_B dv / EW_{abs}$ using the data from Table 2.

³The spin temperature, T_s , computed in the traditional fashion, for optically-thin clouds, $T_s(v_0) = T_B(v_0) / (1 - e^{-\tau(v_0)}) = T_B(v_0) / \tau(v_0)$ when $\tau \ll 1$. T_B is the brightness temperature at velocity v_0 in the emission spectrum, and τ the optical depth at the same velocity. We take v_0 to be the center velocity in the case of individual Gaussian component.